MATERIALS SCIENCE

Regulation of macrophage polarization through surface topography design to facilitate implant-to-bone osteointegration

Yizhou Zhu[1,2,3†], Hang Liang[4†], Xiangmei Liu[2*], Jun Wu[3], Cao Yang[4*], Tak Man Wong[1,3], Kenny Y. H. Kwan[1,3], Kenneth M. C. Cheung[1,3], Shuilin Wu[5], Kelvin W. K. Yeung[1,3,6*]

Copyright © 2021 The Authors, some rights reserved; exclusive licensee American Association for the Advancement of Science. No claim to original U.S. Government Works. Distributed under a Creative Commons Attribution NonCommercial License 4.0 (CC BY-NC).

Proper immune responses are critical for successful biomaterial implantation. Here, four scales of honeycomb-like TiO_2 structures were custom made on titanium (Ti) substrates to investigate cellular behaviors of RAW 264.7 macrophages and their immunomodulation on osteogenesis. We found that the reduced scale of honeycomb-like TiO_2 structures could significantly activate the anti-inflammatory macrophage phenotype (M2), in which the 90-nanometer sample induced the highest expression level of CD206, *interleukin-4*, and *interleukin-10* and released the highest amount of *bone morphogenetic protein-2* among other scales. Afterward, the resulting immune microenvironment favorably triggered osteogenic differentiation of murine mesenchymal stem cells in vitro and subsequent implant-to-bone osteointegration in vivo. Furthermore, transcriptomic analysis revealed that the minimal scale of TiO_2 honeycomb–like structure (90 nanometers) facilitated macrophage filopodia formation and up-regulated the Rho family of guanosine triphosphatases (*RhoA, Rac1, and CDC42*), which reinforced the polarization of macrophages through the activation of the RhoA/Rho–associated protein kinase signaling pathway.

INTRODUCTION

Osteoimmunomodulation orchestrates the process of osteointegration by mediating the response of immune cells and the subsequent behaviors of bone cells (*1*). Upon implantation, the innate immune system of the host can be activated at the interface of the implanted biomaterial within hours (*2*). This inevitable immune response generates an immune environment adjacent to the implanted biomaterials that determines the fate of bone-implant integration. Thus, implantable biomaterials with favorable immune responses can guide the success of osteointegration (*3*).

Macrophages are among the earliest arrivals to interact with the implanted materials, which initiate and mediate the host foreign body response (*4*). Macrophages can perform diverse functions with remarkable plasticity, polarizing to M1 (proinflammatory) or M2 (anti-inflammatory) phenotypes in response to variable local microenvironments. M1 macrophages are known to intensify the inflammatory response by secreting proinflammatory cytokines, such as *tumor necrosis factor*–α (*TNF*-α) and *interleukin-1*β (*IL-1*β) (*5*, *6*). Although M1 macrophages facilitate the recruitment of reparative cells [i.e., mesenchymal stem cells (MSCs)] to the injury site (*7*, *8*), a prolonged presence of M1 macrophages may lead to fibrotic scar tissue formation and tissue injury (*9*, *10*). In contrast, M2 macrophages alleviate inflammation and facilitate tissue repair by producing these cytokines as *IL-4* and *IL-10* (*11*, *12*). A switch to the M2 phenotype has been shown to be essential for bone healing and osteointegration around implants (*13*–*15*). Therefore, the polarization between M1 and M2 macrophages is of paramount importance to determine the success of implant-to-bone osteointegration (*16*–*18*).

Emerging evidence indicates that surface topographical cues are essential to facilitate osteointegration when the osteoimmune tissue microenvironment is properly modulated (*19*–*23*). A previous study demonstrated that surface topography cues are critical for mediating macrophage polarization by modulating cell shapes (*24*). Other researchers also found that micropatterns could induce M2 macrophage polarization when the cells were elongated by the specific patterns (*25*–*27*). However, it has been reported that TiO_2 nanotubes with a diameter of 30 nm suppress cell elongation. The same pattern promoted M2 macrophage activation as compared with TiO_2 nanotubes with an 80-nm diameter (*28*). To date, the underlying mechanism of how surface topographical cues modulate immune cell behaviors is still not known.

To understand the immunomodulatory role of immune cells on surface topographical cues for implant-to-bone osteointegration, we designed a series of specific honeycomb-like surface structures on titanium (Ti) substrates ranging from the nanometer to micrometer scale that could mimic various spatial confinements to the cells. The activation and polarization of RAW 264.7 macrophages on different honeycomb-like structures were systematically examined by the evaluations of cell morphological change, polarization, and secretion of cytokines. Then, we conditionally cultured the MSCs with the macrophage cytokines induced by different scales of honeycomb-like TiO_2 structures in vitro. The immunomodulated osteogenic effect was further illustrated by implanting the Ti rods with various honeycomb-like TiO_2 surface structures in animal models. Last, gene expressions and signaling pathways of macrophages cultured on different samples were studied using transcriptomic analysis.

[1]Department of Orthopaedics & Traumatology, Li Ka Shing Faculty of Medicine, The University of Hong Kong, Pokfulam, Hong Kong 999077, China. [2]School of Materials Science & Engineering, Hubei University, Wuhan 430062, China. [3]Shenzhen Key Laboratory for Innovative Technology in Orthopaedic Trauma, Department of Orthopaedics and Traumatology, The University of Hong Kong-Shenzhen Hospital, Shenzhen 518053, China. [4]Department of Orthopaedics, Union Hospital, Tongji Medical College, Huazhong University of Science and Technology, Wuhan 430022, China. [5]School of Materials Science and Engineering, the Key Laboratory of Advanced Ceramics and Machining Technology by the Ministry of Education of China, Tianjin University, Tianjin 300072, China. [6]China Orthopaedic Regenerative Medicine Group (CORMed), Hangzhou, China.
*Corresponding author. Email: liuxiangmei1978@163.com (X.L.); caoyangunion@hust.edu.cn (C.Y.); wkkyeung@hku.hk (K.W.K.Y.)
†These authors contributed equally to this work.

RESULTS

TiO_2 honeycomb fabrication and characterization

TiO_2 honeycombs on the Ti surface were fabricated via a customized film transfer method. Briefly, monodispersed polystyrene (PS) spheres were first self-assembled on the surface of $Ti(SO_4)_2$ solution. After a thermal hydrolysis process of $Ti(SO_4)_2$ [$Ti(SO_4)_2 + 2H_2O \rightarrow TiO_2 + 2H_2SO_4$], a layer of TiO_2 was formed at the bottom of the monolayered PS film. Subsequently, the as-prepared TiO_2-PS hybrid monolayer was carefully transferred onto Ti substrates. Last, a calcination process was conducted for PS sphere template scarification and TiO_2 crystallization. The obtained TiO_2 honeycomb–like patterns were labeled HC-90, HC-500, HC-1000, and HC-5000 on the basis of the diameter of PS spheres used as the sacrificed templates.

Figure 1A shows the surface topography of different samples under scanning electron microscopy (SEM). The diameter distribution of obtained TiO_2 honeycombs is shown in Fig. 1B, indicating an increasing trend of the mean diameters of HC-90, HC-500, HC-1000, and HC-5000. Figure 1C shows the x-ray diffractometry (XRD) patterns; all the honeycomb samples and unpatterned Ti surface exhibited typical TiO_2 peaks, indicating that the surface phase of all the samples was anatase TiO_2. Figure 1D shows that all TiO_2 honeycombs exhibited improved hydrophilicity compared to the unpatterned Ti surface. Macrophages are highly sensitive to soluble factors, and different materials may also influence macrophage phenotype polarization (*4*). Hence, we constructed TiO_2 honeycombs with different diameters but sharing similar anatase TiO_2 composition and high hydrophilicity. Hence, this experimental setup enables us to isolate the modulatory role of surface topography on the osteoimmune response while largely excluding interference factors such as soluble factors and biochemical factors.

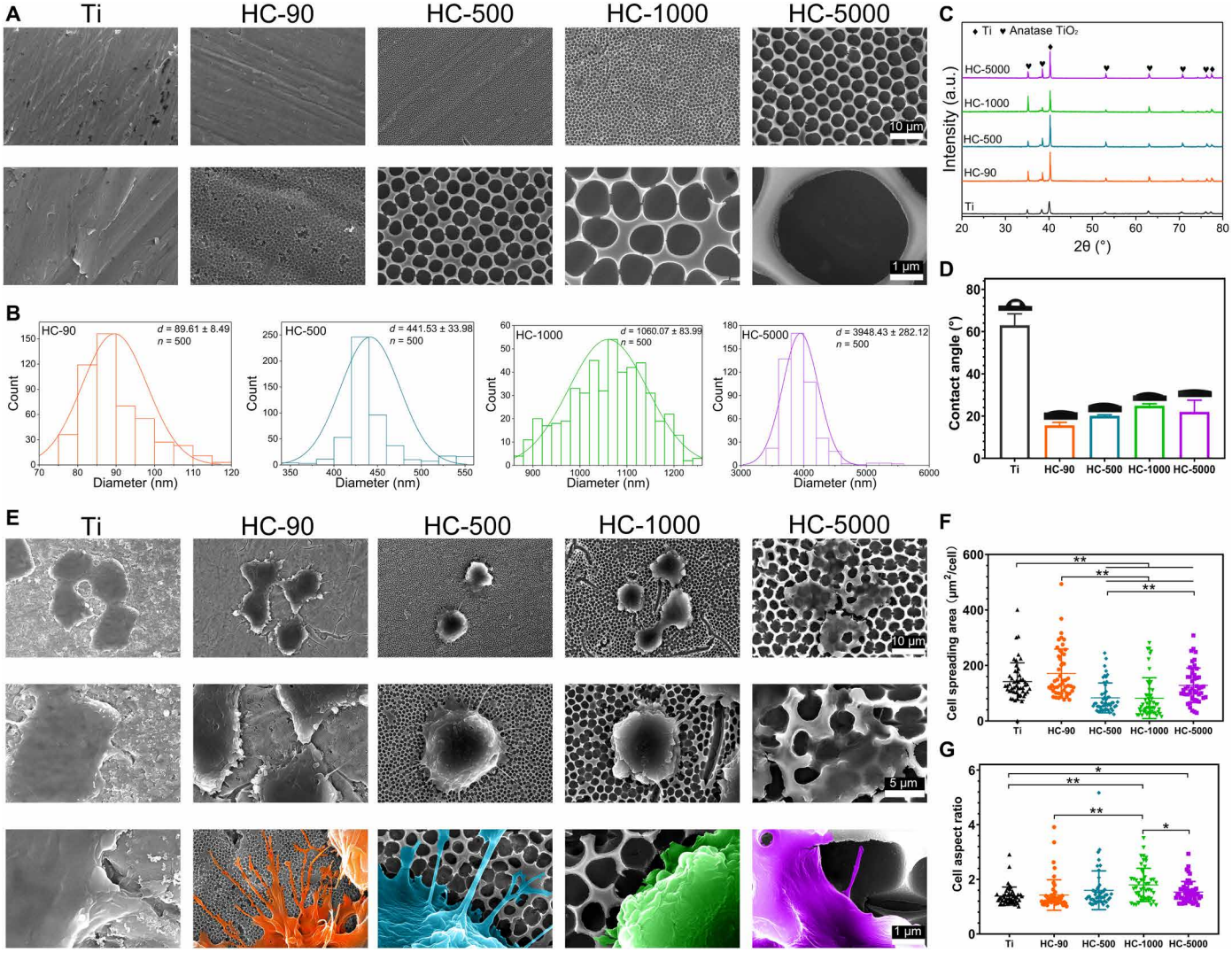

Fig. 1. Surface characterizations of TiO_2 honeycomb–like nanostructures and the morphological changes of macrophages on corresponding surfaces. (**A**) Surface morphologies of different samples under SEM; Scale bars, 10 μm (first panel) and 1 μm (second panel). (**B**) Diameter distribution of different TiO_2 honeycombs. (**C**) XRD patterns of different samples. a.u., arbitrary units. (**D**) Contact angles of different samples. (**E**) Cell morphologies of macrophages on different samples; Scale bars, 10 μm (first panel), 5 μm (second panel) and 1 μm (third panel). (**F**) Quantitative cell spreading area based on SEM images. (**G**) Quantitative cell aspect ratio based on SEM images. $n = 3$ independent experiments per group; $^*P < 0.05$ and $^{**}P < 0.01$.

Morphology change and activation of macrophages on different samples

To explore the influence of TiO_2 honeycombs on macrophages, we seeded RAW 264.7 macrophages on different TiO_2 honeycombs with unpatterned Ti as the control group for 48 hours. First, SEM was applied to observe the cell morphology and ultrastructures of cells on different samples. As shown in Fig. 1E, RAW 264.7 macrophages exhibited distinctive cell morphologies on different samples. Compared with the cells on unpatterned Ti substrate with smooth boundaries, abundant filopodia with long stretching distances were found on HC-90. These filamentous ultrastructures stretched out along the boundary of cells and spread across TiO_2 honeycombs on HC-90. Similarly, protruded filopodia were found on HC-500. However, the number was decreased compared with HC-90. When further increasing the diameter of TiO_2 honeycombs to the micrometer scale, cellular protrusion in terms of filopodia formation was confined, and extended filaments were hardly observed. On HC-5000, the cells seem to be particularly "embedded" into the TiO_2 honeycomb structure. The possible reason for different cellular protrusion behavior and morphology changes could be the different spatial confinement provided by honeycombs with different scales (*29*, *30*). The interval space of HC-90 is only 90 nm, which is smaller than the size of the pseudopodium of cells. In addition, smaller TiO_2 honeycombs with denser nanostructures may provide more anchor points for cells. Thus, cells can easily spread or protrude across the surface topographies on HC-90, forming an abundance of filopodia. For HC-500, the interval space was increased to 500 nm, which is more difficult for macrophages to spread across, but it can still be reached. When further increasing the scale of honeycombs on the Ti surface, the obstacle effect of surface topographies for cell spreading became more notable, which hampered filopodia formation.

Quantitative cell spreading area and cell aspect ratio based on SEM images (fig. S1) are shown in Fig. 1 (F and G). Cells on HC-90 exhibited a higher spreading area than the other three TiO_2 honeycombs. Despite the cell aspect ratio varying from group to group, no correlation was found between aspect ratio variation and the scale of TiO_2 honeycombs. These results revealed that increasing the scale of TiO_2 honeycombs can confine cell spreading and result in distinctive cell morphologies with restricted filopodia formation. Previous studies have demonstrated that cell morphological changes induced by topographical cues can mediate macrophage phenotypes (*25*–*28*). Thus, we next investigated whether TiO_2 honeycombs that induced cell morphology changes can modulate macrophage polarization.

The key hypothesis of this study is that TiO_2 honeycomb structures with different scales can modulate macrophage polarization, and secret cytokines contribute to osteointegration. To verify this, immunofluorescent staining was first applied to explore whether TiO_2 honeycombs can induce macrophage polarization. Inducible nitric oxide synthase (iNOS), an important marker of M1 macrophage activation, is located in the cytoplasm (*31*); CD206, a highly expressed cell-surface protein on M2 macrophages, is a marker for M2 polarization (*32*, *33*). Therefore, iNOS and CD206 were selected for immunofluorescent staining. Figure 2 (A and B) shows the results of immunofluorescent staining images and the quantitative fluorescence intensity. HC-90 exhibited the highest level of CD206. Another TiO_2 honeycomb at the nanometer scale (HC-500) also exhibited much higher levels of CD206 than other groups, indicating that HC-90 and HC-500 can induce M2 macrophage activation. A decreasing trend in the semiquantified fluorescence intensity of CD206 was found with increasing scales of TiO_2 honeycombs. However, no significant difference was found in the M1 marker iNOS among the four groups of TiO_2 honeycombs. The quantitative cell nucleus aspect ratio showed no correlation to the trend of TiO_2 honeycomb diameter variation and activation of macrophage polarization (Fig. 2C).

To further confirm the phenotypes of polarized macrophages on different samples, C─C chemokine receptor type 7 (CCR7), a surface marker of M1 macrophages, and CD206 were selected to evaluate macrophage polarization by flow cytometry analysis. As shown in Fig. 2D, unpatterned Ti exhibited the highest proportion of M1 macrophages (41.7%). The proportion of M1 macrophages on different TiO_2 honeycombs showed the following trend: HC-90 (7.04%) < HC-500 (11.5%) < HC-1000 (18.9%) < HC-5000 (29.4%). In comparison, the proportion of M2 macrophages on TiO_2 honeycombs exhibited the opposite trend: HC-90 (32.7%) > HC-500 (25.8%) > HC-1000 (12.8%) > HC-5000 (8.43%). This indicates that HC-90 could significantly induce M2 macrophage polarization and reduce M1 macrophage polarization compared with unpatterned Ti as the control (CD206 proportion: 24.4%). Figure 2 (E and F) shows the results of M1 and M2 macrophage–related gene expression levels, respectively. Corresponding to the results mentioned above, nanometer-scaled TiO_2 honeycombs exhibited lower expression levels of M1-related genes (*IL-1*β and *TNF-*α) but higher M2-related genes (*IL-4* and *IL-10*) compared with micrometer-scaled TiO_2 honeycombs and unpatterned Ti. Here, NH-90 exhibited the lowest expression level of M1 macrophage genes but the highest M2 macrophage genes.

In addition to regulating inflammatory environments, macrophages can mediate bone regeneration by secreting osteoinductive factors (*11*, *17*). For example, *bone morphogenetic protein-2* (*BMP-2*) and *oncostatin M* (*OSM*) are potent inducers of osteogenesis secreted by macrophage (*34*, *35*). The expression levels of *BMP-2* and *OSM* of macrophages cultured on different samples are shown in Fig. 2G. We found that the tendency of expression levels of *BMP-2* on different samples was like that of M2 macrophage genes (*IL-4* and *IL-10*). HC-90 and HC-500 exhibited a higher expression level of *BMP-2* than other groups, with HC-90 showing the highest level. However, no significant difference was found in the expression level of *OSM*.

We next analyzed the secretion of macrophage-associated cytokines using enzyme-linked immunosorbent assay (ELISA). The results are shown in Fig. 2 (H to J), illustrating good concordance with the results mentioned above; macrophages on TiO_2 honeycombs at the nanometer scale (HC-90 and HC-500) secreted lower amounts of proinflammatory cytokines (*IL-1*β and *TNF-*α) but higher amounts of anti-inflammatory cytokines (*IL-4* and *IL-10*). In accordance with the above results, HC-90 and HC-500 showed a significantly higher level of *BMP-2*, while no significant difference was found in *OSM* secretion. Zhang *et al.* (*36*) found that *OSM* is secreted by M1 macrophages, while higher *BMP-2* secretion was attributed to M2 macrophages. Similarly, our results demonstrated that *BMP-2* production was increased on HC-90 and HC-500, on which macrophages were polarized to M2 phenotypes.

Macrophage cytokines modulate osteogenic differentiation of MSCs in vitro

To explore the regulatory role of macrophage cytokines on osteogenic differentiation of MSCs, RAW 264.7 macrophages were first seeded on different samples for 48 hours. The supernatant was

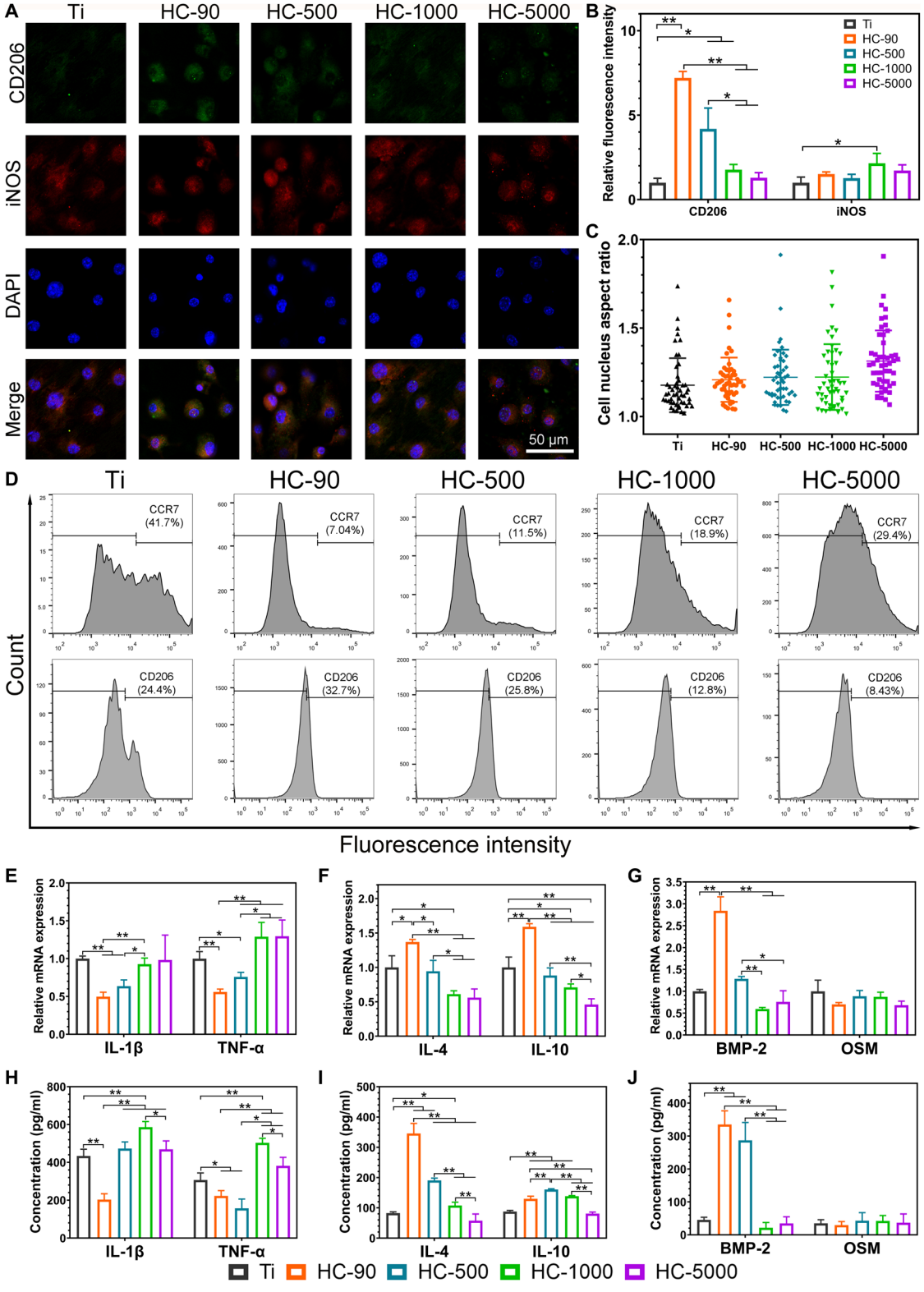

Fig. 2. In vitro immune responses of macrophages on various nanostructures. (**A**) Fluorescence microscopy images of CD206, iNOS, and nucleic staining of macrophages on different samples. (**B**) Quantitative fluorescence intensity of CD206 and iNOS of macrophages on different samples. (**C**) Quantitative cell nucleus aspect ratio based on fluorescence microscopy images. (**D**) Polarization of macrophages was evaluated by the expressions of CCR7 (M1) and CD206 (M2) using flow cytometry. (**E**) Relative mRNA expression levels of M1 macrophage–related genes *IL-1*β and *TNF-*α. (**F**) Relative mRNA expression level of M2 macrophage–related genes *IL-4* and *IL-10*. (**G**) Relative mRNA expression level of osteogenic-related genes *BMP-2 and OSM*. (**H**) ELISA analyses of proinflammatory cytokines *IL-1*β and *TNF-*α. (**I**) ELISA analyses of anti-inflammatory cytokines *IL-4* and *IL-10*. (**J**) ELISA analyses of pro-osteogenic cytokines *BMP-2* and *OSM*. $n = 3$ independent experiments per group; $^{*}P < 0.05$ and $^{**}P < 0.01$.

collected to investigate how macrophage polarization induced by TiO_2 honeycombs influences the osteogenic differentiation of MSCs.

To exclude the effect of surface topography on osteogenic differentiation of MSCs, we first measured the alkaline phosphatase (ALP) activity of MSCs cultured on different samples without macrophage cytokines. HC-90 exhibited slightly increased ALP activity (Fig. 3A). However, when we supplemented cytokines collected from macrophages, the ALP activity of HC-90 with macrophage cytokines increased markedly compared with HC-90 without macrophage cytokines. As shown in Fig. 3B, this activity was approximately two times greater than that of other groups at days 7 and 14, exhibiting the highest ALP activity. As ALP is an early marker for osteogenic differentiation (*37*), these results indicate that cytokines collected from macrophages cultured on HC-90 could induce rapid osteogenic differentiation of MSCs. We further evaluated the expression level of three typical osteogenic-related genes, namely, *ALP*, *runt-related transcription factor 2 (Runx2)*, and *osteocalcin* (*OCN*). The results are shown in Fig. 3C. HC-90 exhibited much higher expression levels of *ALP*, *Runx2*, and *OCN* than the other groups did at both days 7 and 14. Moreover, HC-90 exhibited the highest extracellular matrix (ECM) mineralization (Fig. 3, D and E), providing further evidence that HC-90 could significantly promote osteogenic differentiation of MSCs. It has been reported that the host immune response is essential for osteointegration (*38*). In the present study, it was found that HC-90–induced M2 macrophages secrete the cytokines *IL-10*, *IL-4*, and *BMP-2*, which, in turn, promote the osteogenic differentiation of MSCs (*11*, *12*, *39*).

HC-90 promotes osteointegration in vivo

The above in vitro results demonstrated the scale dependence of the modulatory role of TiO_2 honeycombs in macrophage polarization and osteogenic differentiation of MSCs. HC-90 can induce macrophages into a proregenerative M2 phenotype and promote the highest osteogenic differentiation of MSCs in vitro. Therefore, to further

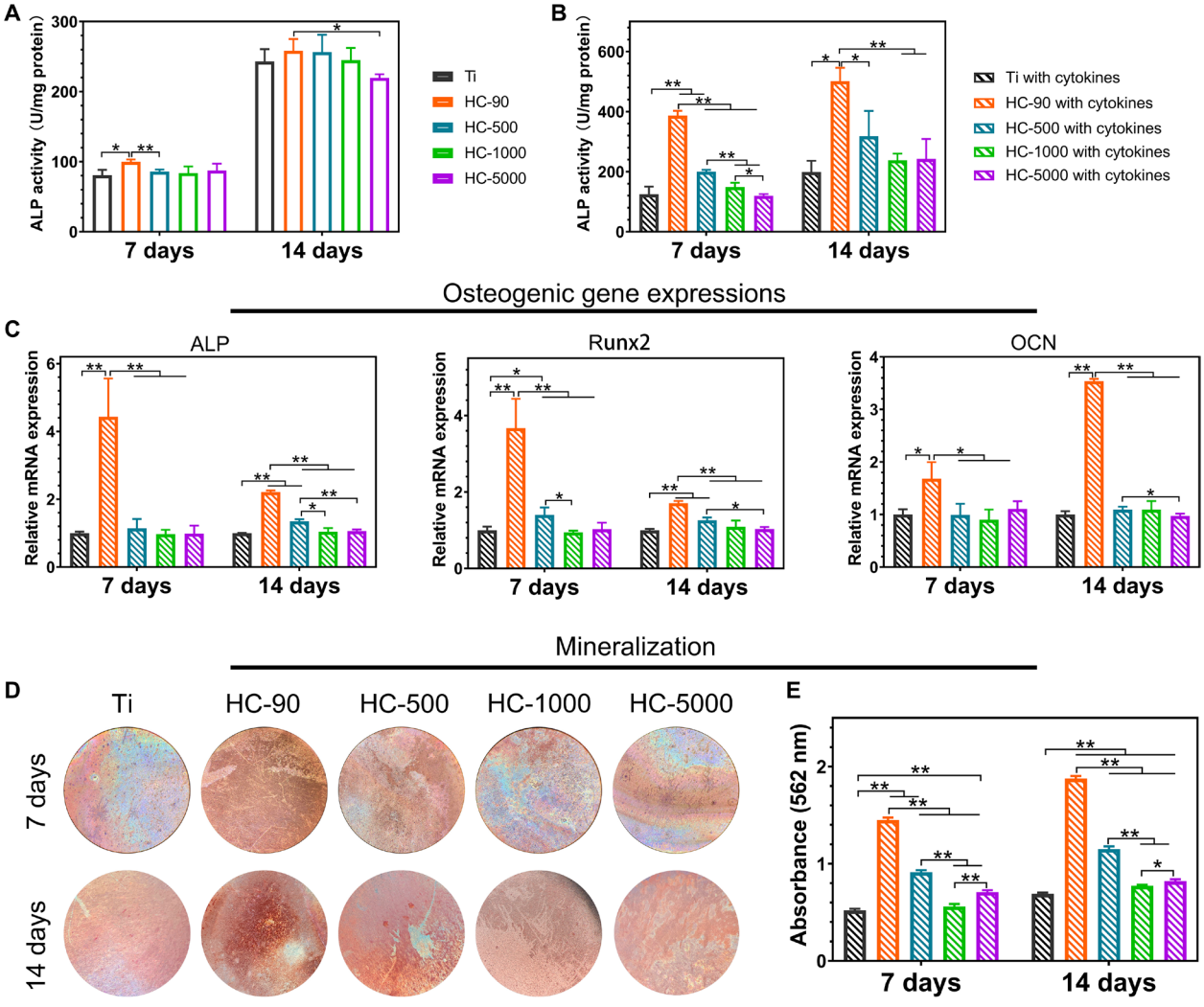

Fig. 3. In vitro osteogenic differentiation behaviors of MSCs on various nanostructures. (**A**) ALP activity of MSCs cultured on different samples without macrophage cytokines. (**B**) ALP activity of MSCs cultured on different samples with macrophage cytokines collected from corresponding samples. (**C**) Relative expression level of *ALP*, *Runx2*, and *OCN* of MSCs cultured on different samples with macrophage cytokines collected from corresponding samples. (**D**) Optical images of Alizarin Red staining of MSCs cultured on different samples with macrophage cytokines collected from corresponding samples. Photo credit: Y.Z., The University of Hong Kong. (**E**) Quantitative analysis of Alizarin Red staining. $n = 3$ independent experiments per group; $^{*}P < 0.05$ and $^{**}P < 0.01$.

investigate whether the TiO_2 honeycombs could affect osteointegration around implants in vivo, we selected HC-90 and HC-5000, the minimum- and maximum-scaled TiO_2 honeycombs, respectively, to conduct a rat tibia implantation model. The adhesions of fibrinogen and vitronectin on HC-90 surface were significantly higher as compared with other samples after 8 hours of surgery (Fig. 4A). Fibrinogen is one of the most abundant proteins in blood plasma, and its adhesion on biomaterial surface has been proven to be crucial on macrophage

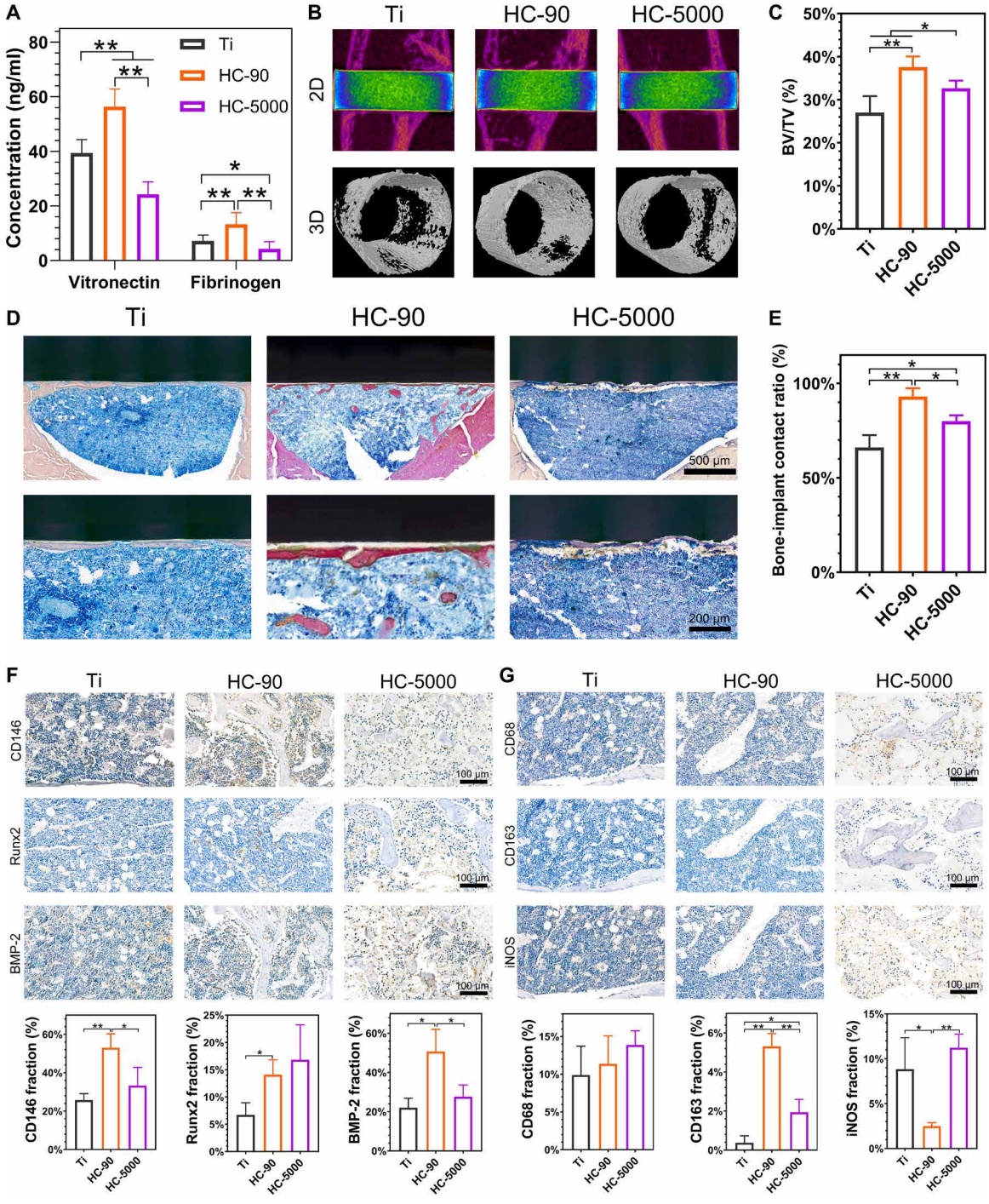

Fig. 4. In vivo implant-to-bone osteointegration of HC-90 and HC-5000 surfaces. (**A**) Protein absorption on implant surfaces after 8 hours of surgery. (**B**) 2D and 3D micro-CT images of tissue at the site of implantation. (**C**) Quantitative analysis of the newly formed bone volume around the implants (BV/TV). (**D**) Van Gieson's picrofuchsin staining of tissue around the implants. (**E**) Bone-implant contact ratio. (**F**) Representative immunohistochemical images of CD146, Runx2, and BMP-2 in defect areas, and semiquantification of positively stained cells. (**G**) Representative immunohistochemistry staining of CD68, CD163, and iNOS in defect areas and semiquantification of positively stained cells. $n = 3$ independent experiments per group; $^*P < 0.05$ and $^{**}P < 0.01$.

recruitment (*40*, *41*). Besides, the literature reported that absorbed fibrinogen could induce monocytes and macrophages to produce osteogenic growth factors, e.g., BMPs, that might convince osteogenesis (*42*). A previous study also reported that the absorption of vitronectin could facilitate the attachment of osteoblastic cells (*43*). Thus, the protein absorption on HC-90 surface may also facilitate bone-to-implant osteointegration in vivo.

After 4 weeks, the implanted samples were harvested to evaluate osteointegration in vivo. Figure 4B shows the two-dimensional (2D) and 3D reconstructed micro–computed tomography (CT) images. The highest degree of new bone formation was observed on HC-90, which was further confirmed by the quantified bone volume fraction (BV/TV; Fig. 4C). Figure 4D shows the results of Van Gieson's picrofuchsin staining; bone tissues (red) were visualized at the bone-implant interface. The newly formed bone was directly in direct contact with HC-90, with a higher bone-implant contact ratio compared with other groups (Fig. 4E). These results further confirmed that HC-90 could effectively promote osteointegration not only in vitro but also in vivo.

Previous studies have demonstrated that MSCs mobilized from bone marrow can be recruited to the implantation area and differentiate into osteoblasts for bone regeneration (*44*, *45*). Thus, the recruitment of host stem cells to the bone-implant interface is crucial for osteointegration. To understand how the TiO_2 honeycombs affect the local microenvironment and contribute to osteointegration around implants, we next conducted immunohistochemistry staining in series to visualize MSCs and macrophages in the harvest tissues. The immunohistochemistry staining images of MSCs and the semiquantitative results are shown in Fig. 4F. CD146 is a surface marker for MSCs; the number of $CD146^+$ cells in the HC-90 group was higher than that in HC-5000 and unpatterned Ti. In addition, more Runx2 and BMP-2 positive cells were found in HC-90. These results indicate that HC-90 could simultaneously increase recruitment and promote osteogenesis of MSCs, which is consistent with the in vitro results described above. As shown in Fig. 4G, more $CD163^+$ M2 macrophages were found in HC-90, whereas a larger number of $iNOS^+$ M1 macrophages were found in HC-5000. These results indicate that HC-90 implantation could induce M2 macrophage polarization, providing a favorable anti-inflammatory microenvironment for the osteointegration process and facilitating osteointegration in vivo.

Surface confinement modulates filopodia formation and macrophage polarization

As described above, morphologies of RAW 264.7 macrophages varied on TiO_2 honeycombs with different scales (Fig. 1E). Macrophages probed different TiO_2 honeycomb surface topographies and responded to spatial confinement with different numbers of filopodia. As shown in SEM images (Fig. 1E), macrophages on TiO_2 honeycombs at the nanometer scale exhibited a greater abundance of filopodia, while almost no filopodia were found on TiO_2 honeycombs at the micrometer scale. The modulatory role of TiO_2 honeycombs on macrophage polarization exhibited a similar scale dependence. That is, TiO_2 honeycombs with smaller diameters at the nanometer scale, especially HC-90, induced macrophages with the M2 phenotype via more *BMP-2* cytokine secretion but alleviated M1 macrophage activation (Fig. 2). Despite some differences in the cell aspect ratio and cell nucleus aspect ratio (Figs. 1G and 2C), the observed M2 macrophage activation rates elicited by HC-90 and HC-500 were not consistent with the "elongation rules" reported in previous studies (*25*–*27*). No direct correlation was found between macrophage phenotypes and cell elongation in our study. The most notable difference in terms of cell morphology changes was found in filopodia formation: HC-90 exhibited both the most abundant filopodia and the highest expression level of M2 macrophage genes. In addition, compared with two TiO_2 honeycombs at the micrometer scale (HC-1000 and HC-5000), HC-500—with more filopodia—also induced M2 macrophage activation. Thus, we suspect that the formation of filopodia on different samples may be important for modulating macrophage polarization.

To understand how TiO_2 honeycombs activate macrophage polarization, transcriptomic analysis of macrophages cultured on different samples was applied. First, the Pearson correlation between samples was used to assess the specimen's stability through the correlation analysis. Most of the correlation coefficients were within acceptable ranges ($R^2 > 0.92$; Fig. 5A). Figure 5B shows that there were many differences in gene expression when comparing different TiO_2 honeycombs with unpatterned Ti (2650 genes in HC-90 versus Ti, 1255 genes in HC-500 versus Ti, 1393 genes in HC-1000 versus Ti, and 1440 genes in HC-5000 versus Ti), and they shared 899 genes. Our results have demonstrated that the modulatory role of TiO_2 honeycombs is scale dependent. In addition, the transcriptomic analysis revealed that the number of differentially expressed genes between two groups with adjacent scales (HC-500 versus HC-90, HC-1000 versus HC-500, and HC-5000 versus HC-1000) was not significant [shown in volcano plots in Fig. 5 (C to E) and summarized in table S1]. Thus, we compared HC-90 (minimum diameter), HC-5000 (maximum diameter), and unpatterned Ti as the control group using pairwise comparison. As shown in Fig. 5 (F to H), the volcano plots showed 713 up-regulated and 1937 down-regulated genes (HC-90 versus Ti), 589 up-regulated and 851 down-regulated genes (HC-5000 versus Ti), and 344 up-regulated and 125 down-regulated genes (HC-5000 versus HC-90), indicating a wide range of gene expression differences. The differentially expressed genes were collected to perform Gene Ontology (GO) database analysis. All differential genes were typically divided into three typical classes, including biological process (BP), molecular function (MF), and cellular component (CC). The top 20 enriched terms of HC-90 versus Ti are shown in Fig. 6A. Genes were rich in the regulation of cytoplasm and cytoskeleton, which correlated with the morphological changes of macrophages induced by surface topography on HC-90. Then, the Kyoto Encyclopedia of Genes and Genomes (KEGG) was performed to analyze the underlying signaling pathways. The top enriched up-KEGG pathways are shown in Fig. 6B. In addition to cell adhesion molecules (CAMs), peroxisome proliferator-activated receptor (PPAR) signaling pathways were up-regulated, which has been demonstrated to be related to M2 macrophage activation (*46*). In comparison, M1 macrophage activation–related pathways [i.e., mitogen-activated protein kinase (MAPK), TNF, nuclear factor κ light chain enhancer of activated B cells, and nucleotide-binding oligomerization domain (NOD)–like receptor signaling pathways] were down-regulated (*47*–*50*). The experimental variable in our study is the physical topography cues induced by TiO_2 honeycombs with different diameters. Therefore, we next focus on the differences in surface topography-induced gene expressions, including cell adhesion, cytoskeleton arrangement, and subsequent mechanotransduction genes. These differential gene expressions are shown in the resulting heatmap (Fig. 6C).

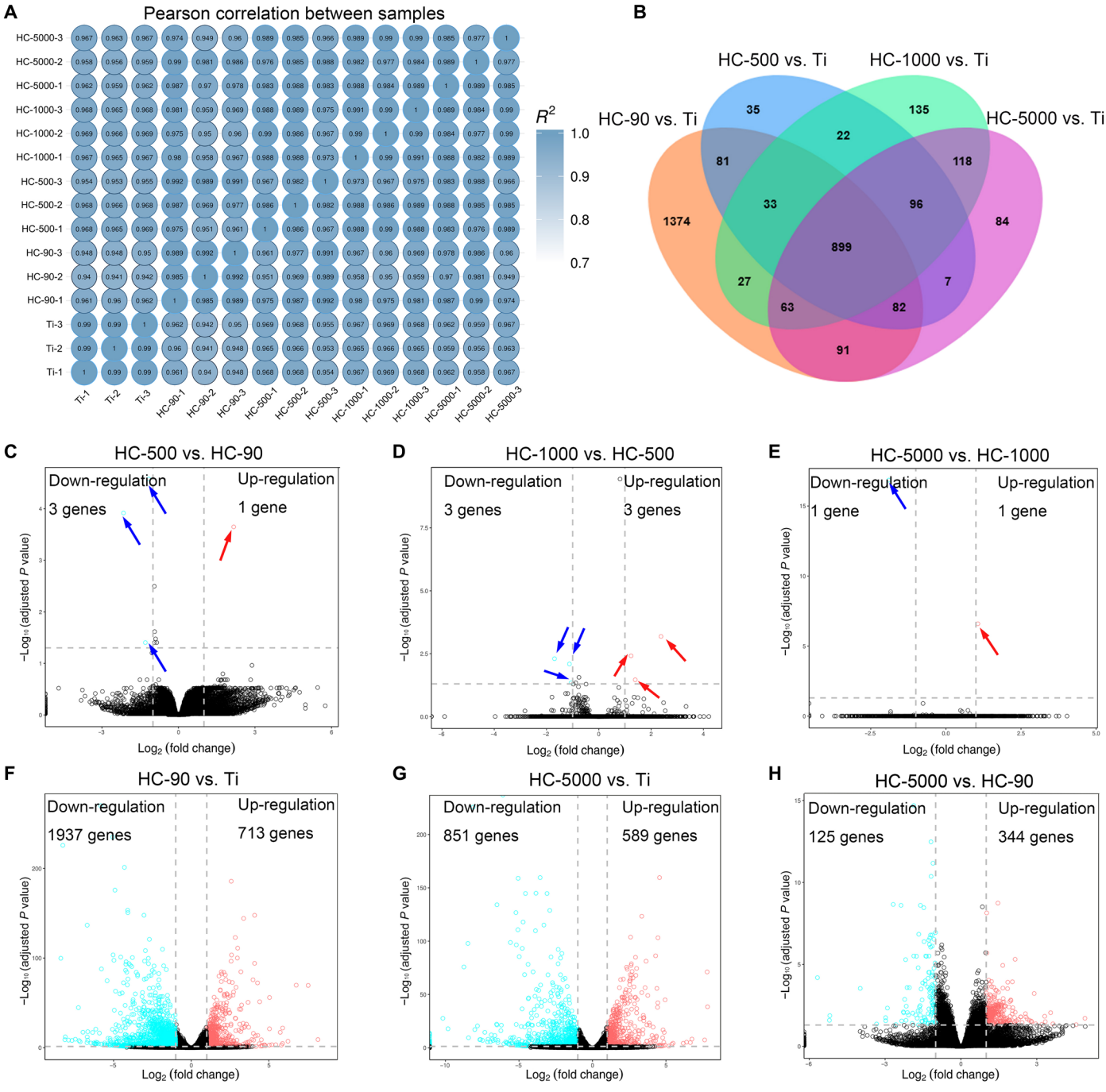

Fig. 5. Bioinformatic analysis of macrophage gene expression on various nanostructures. (**A**) Heatmap of Pearson correlation between samples. (**B**) Venn diagram of the number of differentially expressed genes in different TiO_2 honeycombs compared with unpatterned Ti. (**C** to **H**) Volcano plot of transcriptomic analysis of differentially expressed genes. $n = 3$ independent experiments per group.

For macrophages to be activated by surface topographies, they must be able to sense and respond to extracellular cues, transducing biochemical signals to modulate gene expression. Cell protrusions (i.e., filopodia) serve as an "antenna" in this process. They are linked to cell motility and migration, which are required for several processes of macrophages that occur during immunity and inflammation processes in fighting infection (*51*). As illustrated in Fig. 6D, the interaction between macrophages and the ECM begins with cell adhesion, which is mainly mediated by integrins (*52*). Integrins have been reported to be involved in cell adhesion and podosome formation and to influence macrophage activation (*53*–*55*). For example, inhibition of *integrin* β1 can lead to a block of M2 macrophage polarization (*56*). Once adherent, additional proteins (i.e., *vinculin*, *paxillin*, *talin*, and *Src*) are recruited and assembled to form focal

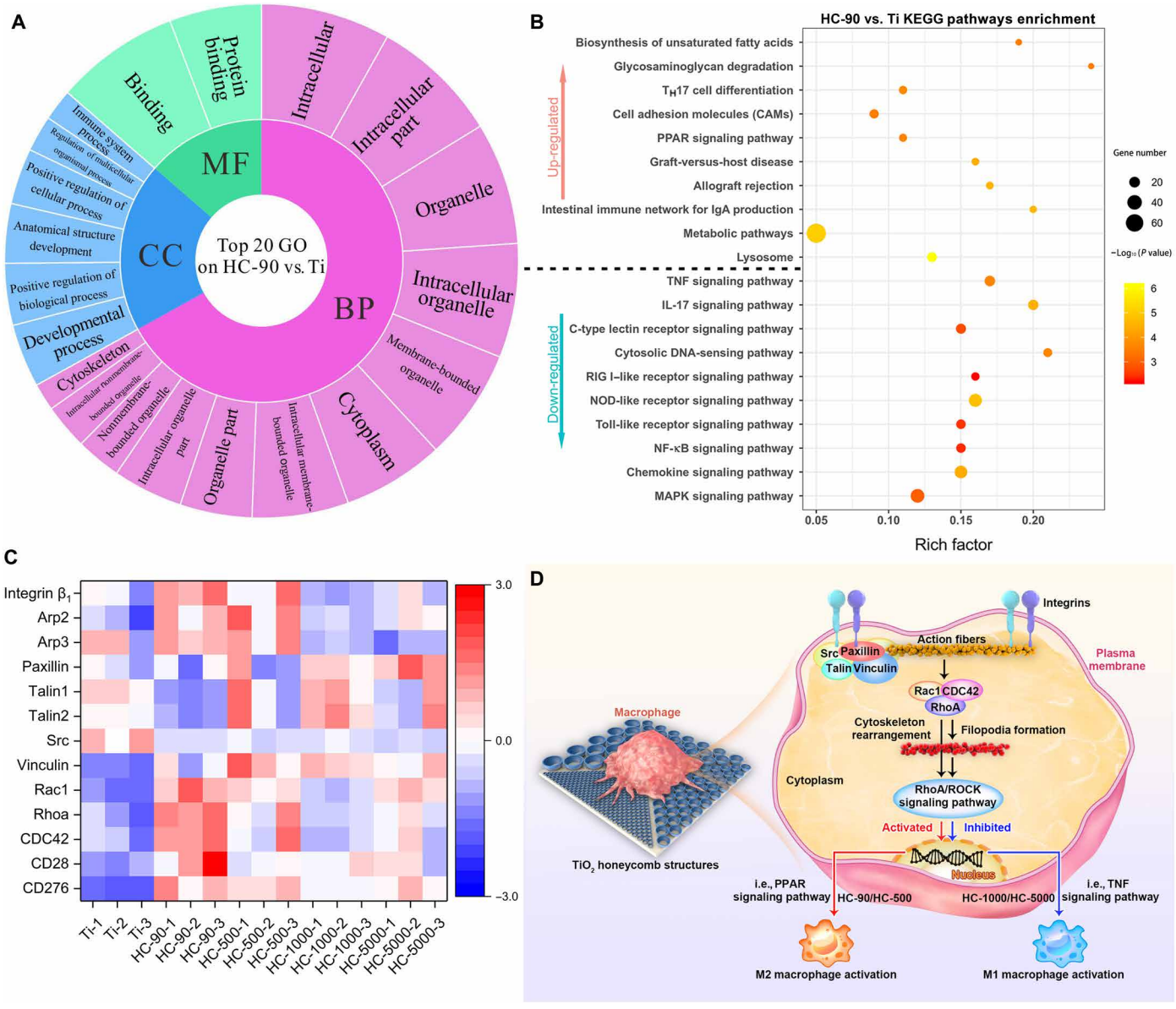

Fig. 6. Mechanistic analysis of macrophage polarization induced by TiO_2 honeycomb–like nanostructures. (**A**) GO analysis of all genes in macrophages cultured on HC-90 versus unpatterned Ti. (**B**) Enriched KEGG pathways of HC-90 versus unpatterned Ti. T_H17, T helper 17; IgA, immunoglobulin A; RIG I, retinoic acid-inducible gene I, NF-κB, nuclear factor κB. (**C**) Heatmap analysis of differentially expressed genes involved in cell adhesion, cytoskeleton arrangement, and mechanotransduction. (**D**) Scheme illustration of the mechanism of macrophage polarization on the nanostructures. $n = 3$ independent experiments per group.

adhesions, which serve as the mechanosensors, linking to actin fibers and playing an essential role in signal transduction and modulating gene expressions. While macrophages do not form classical focal adhesions, podosomes dominate cell-matrix contacts (*57*, *58*). Podosomes are actin-rich mechanosensory structures that play a similar role to focal adhesion, but they have a different structure and are more unstable than focal adhesions (*4*). Transcriptomic analysis revealed that genes related to podosome formation and cytoskeleton arrangement were differentially expressed on different samples. We noticed the up-regulation of *Arp2* and *Arp3* on HC-90, which are marker genes mediating podosome formation via actin polymerization (*53*), indicating that HC-90 may facilitate podosome formation. Integrin-binding protein-related genes, such as *paxillin*, *talin*, and *Src*, were down-regulated. This may result in lower cytoskeleton contractility, which has been reported to facilitate podosome formation (*53*). In addition, intracellular tension inevitably affects cytoskeleton rearrangement, subsequent mechanotransduction, and gene expression. For example, a higher cellular elastic modulus was associated with M1 macrophage activation (*4*). Thus, the down-regulation of *paxillin*, *talin*, and *Src* may contribute to the alleviation of the proinflammatory response of macrophages on HC-90.

Downstream of podosome formation is the Rho family of guanosine triphosphatases (GTPases), which has been reported to be involved not only in cell adhesion and spreading but also in the assembly of actin stress fibers (*RhoA*), lamellipodia (*Rac1*), and filipodia (*CDC42*) (*59*). The up-regulation of *RhoA*, *Rac1*, and *CDC42* on

HC-90 and HC-500 promoted cell protrusion and resulted in more filopodia formation by mediating actin-based cytoskeleton rearrangements. The Western blot analysis suggested that the expressions of RhoA [a small upstream GTPase protein of Rho-associated protein kinase (ROCK)] and two specific phosphorylated ROCK substrates [i.e., phosphorylated myosin light chain (p-MLC) and myosin phosphatase target subunit 1 (p-MYPT1)] on HC-90 surface were significantly up-regulated as compared with others (fig. S2), indicating that the RhoA/ROCK signaling pathway had been activated by HC-90 sample (*60*). The essential role of the RhoA/ROCK signaling pathway in M2 macrophage activation has been confirmed by researchers. For example, a recent study found that inhibition of the RhoA/ROCK signaling pathway can result in switching the M2 phenotype to the M1 phenotype (*60*). This agrees with our results that the up-regulation of *RhoA*, *Rac1*, and *CDC42* could activate M2 macrophage polarization–related signaling pathways of macrophages cultured on HC-90 and HC-5000. In contrast, the down-regulation of *RhoA*, *Rac1*, and *CDC42* led to M1 activation of macrophages cultured on HC-1000 and HC-5000.

To summarize, macrophages can sense the surface topography of TiO_2 honeycombs with different scales. The smaller scale of TiO_2 honeycombs, especially for HC-90, provided minor spatial confinement but more anchor points for cells. In response to this surface topographical cue, the Rho family of GTPases (*RhoA*, *Rac1*, and *CDC42*) was up-regulated. The up-regulation of these genes was intuitively exhibited in cell morphology changes involving a more abundant formation of filopodia. The activation of the RhoA/ROCK signaling pathway is correlated with M2 macrophage polarization. We assume that a surface topography with the ability to facilitate the formation of filopodia can shift macrophages toward M2 polarization.

DISCUSSION

This study developed TiO_2 honeycomb–like structures on Ti surfaces with different scales to investigate the modulatory role of surface topography on macrophage polarization. The mechanism of how physical topography cues modulate macrophage polarization and promote bone regeneration was elucidated in the present study. In summary, manipulating the scale of TiO_2 honeycombs can regulate macrophage polarization and cytokine secretion, modulating the local immune environment, which eventually facilitates new bone formation and osteointegration. Specifically, TiO_2 honeycombs on the Ti surface at the nanometer scale, HC-90 especially, enabled macrophages to overcome the surface spatial confinement, facilitating the formation of filopodia. The abundant filopodia formation was attributed to the up-regulation of the Rho family of GTPases, which activated the RhoA/ROCK signaling pathway and eventually induced M2 macrophage activation. The proper immune microenvironment provided by HC-90 not only can promote osteogenic differentiation of MSCs in vitro but also can facilitate bone-to-implant osteointegration in vivo. Despite this, the interaction between signaling pathways involved in the process needs to be further identified. We believe this study could inspire the design of a new generation of tissue-engineered biomaterials with proper immune responses.

MATERIALS AND METHODS

Sample preparation and characterization

Ti disks of two different sizes (ϕ32 mm by 2.5 mm and ϕ6 mm by 2.5 mm) were obtained from Fu-Tai Metal Materials Co. (China) and Shunhang Metal Materials Co. (China), respectively. The former Ti plates were used for culturing cells for quantitative polymerase chain reaction (qPCR) analysis, ELISA, and transcriptomics, while the latter ones were used for other general tests. First, all Ti disks were mechanically polished using SiC papers of 240, 400, 600, 800, and 1200 grids in a graduated fashion. Subsequently, the polished Ti disks were immersed and ultrasonically cleaned in acetone, ethanol, and deionized water in sequence. Except for collecting the supernatant of macrophages cultured on substrates and qPCR, the Ti disks of 6 mm in diameter were used for other tests. Ti rods (ϕ2 mm by 6 mm) were used for animal experiments. Analytical grade titanium sulfate [$Ti(SO_4)_2$] was bought from Sinopharm Chemical Reagent Co. Ltd. (Shanghai, China). Monodisperse PS spheres with diameters of 90 nm, 500 nm, 1 μm, and 5 μm were obtained from Dae Technology Co. Ltd. (Tianjin, China). Single-side polished silicon wafers were obtained from Zhejiang Lijing Photoelectric Technology Co. Ltd. (Quzhou, China). Silicon wafers were cut into rectangle slides and heated in a H_2SO_4-H_2O_2 mixed solution (v:v = 3:1) for 1 hour to obtain hydrophilic surfaces.

Honeycomb-like patterns with different diameters were prepared on Ti substrates by using monodispersed PS spheres as sacrificed templates. In a typical procedure, PS spheres were first dispersed in equal volumes of ethanol via ultrasonication for 30 min. Then, 50 to 500 μl of the dispersion of PS spheres was dropped on an inclining silicon slide with one side immersed in a ϕ90 mm petri dish containing aqueous $Ti(SO_4)_2$ solution (5.4 weight %). The obtained monolayer PS spheres in the petri dish were kept in an oven at 50°C for 3 hours for TiO_2 deposition onto the bottom of the PS spheres through a thermal hydrolysis process: $Ti(SO_4)_2 + 2H_2O \rightarrow TiO_2 + 2H_2SO_4$. Subsequently, the obtained PS-TiO_2 hybrid spheres were transferred onto Ti substrates and dried overnight at room temperature. Last, the resultant films were calcined at 500°C for 2 hours to remove the PS templates. The obtained samples were named after the size of the PS templates (Ti; 90 nm, 500 nm, 1 μm, and 5 μm). The surface morphology, phase composition, and wettability of different samples were measured using a field-mission SEM (Zeiss Sigma 500, Germany), XRD (D8A25, Bruker, Germany), and a contact angle goniometer (JC2000D2, Powerach, China), respectively.

Macrophage response to different samples in vitro

The RAW 264.7 macrophage cell line and MSCs were obtained from the Union Hospital, Tongji Medical College, Huazhong University of Science and Technology, Wuhan, China. All cells were cultured in a 5% CO_2 atmosphere in an incubator at 37°C. Briefly, RAW 264.7 macrophages were cultured in Dulbecco's modified Eagle's medium (HyClone, USA) containing 1% penicillin-streptomycin solution (Gibco, USA) and 10% fetal bovine serum (FBS) (Gibco), with the medium changed every day. MSCs were cultured in a different growth medium [α–modified Eagle's medium (HyClone, USA):FBS:penicillin-streptomycin = 89:10:1], with the medium changed every 3 days.

All samples were first sterilized using 75% ethanol and then kept under ultraviolet light for 30 min before use. A total of 200 μl or 2 ml of cell suspension RAW 264.7 macrophages (1×10^4 cells/ml) were cultured on different groups of samples ($n = 3$) in 96-well (ϕ6 samples) or 6-well (ϕ32 samples) plates.

Morphological observation of macrophages

RAW 264.7 macrophages were sparsely cultured on different samples for 24 hours, fixed with 2.5% glutaraldehyde for 2 hours, and

then gradient-dehydrated with 30, 50, 70, 90, and 100% ethanol for 15 min in each step. Last, the cell morphologies of different samples were observed under SEM (Zeiss Sigma 500, Germany).

Immunofluorescence staining

RAW 264.7 macrophages cultured on different samples for 48 hours were fixed with 4% paraformaldehyde for 20 min, permeabilized with 0.25% Triton X-100 for 20 min, and blocked by 1% bovine serum albumin for 1 hour. Subsequently, cells in different samples were incubated with the primary antibodies against CD206 (Abcam) and iNOS (Abcam) with 1:100 dilution at 4°C overnight. Then, the cells were further incubated with Alexa Fluor 488 conjugate anti-mouse or Alexa Fluor 594 conjugate anti-mouse secondary antibody for 30 min, followed by 5 min of nuclear staining with 4′,6-diamidino-2-phenylindole (DAPI). The immunofluorescence-stained cells were visualized with a laser scanning confocal microscope (Nikon Instruments Inc., Japan).

Flow cytometry

The surface markers of M1 macrophages (CCR7) and M2 macrophages (CD206) were examined using flow cytometry. Briefly, RAW 264.7 macrophages cultured on different samples were isolated by trypsinization after being cultured for 48 hour and washed with phosphate-buffered saline (PBS) three times. Subsequently, the cells were blocked with CD16/32 for 10 min and then incubated with allophycocyanin-conjugated CCR7 (BioLegend) and phycoerythrin-conjugated CD206 (BioLegend) for 1 hour. Appropriate isotypes were used, and ethidium monoazide bromide staining excluded dead cells. Last, cells were washed with PBS and then analyzed using a flow cytometer (FACSCanto II, Becton-Dickinson). The data were analyzed using FlowJo software.

Quantitative real-time polymerase chain reaction

Total RNA from cells was isolated using an RNA kit (OMEGA, USA) and then reverse-transcribed to cDNA using PrimeScript RT Master Mix (TaKaRa, Japan) following the manufacturer's guidance. Real-time PCR was performed on a Bio-Rad RT-PCR system (Bio-Rad, USA) for internal reference for glyceraldehyde-3-phosphate dehydrogenase (GAPDH), M1 markers *IL-1*β and *TNF*-α, M2 markers *IL-4* and *IL-10*, and immune osteogenesis–related markers *BMP-2* and *OSM*. The primers synthesized are shown in table S2.

Enzyme-linked immunosorbent assay

To measure the cytokine of macrophages on different samples, RAW 264.7 macrophages were first cultured on different samples for 48 hours to collect supernatants. The secretion of cytokines *IL-1*β, *TNF*-α, *IL-4*, *IL-10*, *BMP-2*, and *OSM* were then measured by commercial ELISA kits (Boster Bio, Wuhan, China) following the manufacturer's guidance.

In vitro immunoregulation of osteogenesis of MSCs

RAW 264.7 macrophages were first cultured on different samples for 48 hours to collect supernatants. To investigate the regulatory role of RAW 264.7 macrophages in response to different samples on osteogenesis of MSCs, MSCs were cultured on different samples with supernatants collected from RAW 264.7 macrophages cultured on corresponding samples. The MSCs were observed under a fifth passage and cultured in the culture medium described above but supplemented with supernatant from macrophages at a ratio of 1:1.

ALP activity

To evaluate the influence of macrophage cytokines on the osteogenic differentiation of MSCs, ALP activity assays were first used. MSCs were cultured for 7 and 14 days on different samples with or without adding collected supernatants. After culturing cells for a certain period, the cells on different samples were lysed by adding 100 μl 1% Triton X-100 and cultured in a 37°C water bath for 1 hour. Subsequently, the ALP activity of cells and total protein content were measured using a commercial ALP activity kit (Nanjing Jiancheng Bioengineering Institute, China) and a Bicinchoninic Acid (BCA) protein assay kit (Solarbio, China) according to each manufacturer's guidance. The relative ALP activity of cells in each well was then normalized to the corresponding total protein content.

Osteogenesis-related gene expression

To measure the expression level of typical osteogenic genes of MSCs at days 7 and 14, the same experimental procedure as mentioned above was conducted. The primers for selected genes *ALP*, *Runx2*, and *OCN* are shown in table S2.

Alizarin Red staining

To evaluate the mineralization tendency of MSCs cultured on different samples with the collected supernatants at days 7 and 14, Alizarin Red staining was performed. After culturing cells for a certain period, cells were fixed with 4% paraformaldehyde and then stained with 2% Alizarin Red solution (10 min for each step). The cells were then rinsed thoroughly with PBS to remove excess stain. The images of stained calcium nodules were captured using a digital camera (Phenix XTL-165-VT, Shangrao, China). Last, the mineralized nodules were dissolved in 10% hexadecyl pyridinium chloride and quantified using a microplate reader at 562 nm.

Western blot analysis

RAW 264.7 macrophages were first cultured on different samples for 48 hours. Then, the proteins were extracted using radioimmunoprecipitation assay lysis buffer (Beyotime, Shanghai, China), and the concentration was determined using a BCA protein assay. The amounts of protein were equally fractionated using gel electrophoresis and blotted onto nitrocellulose membranes. After blocked by 5% nonfat milk, the membranes were incubated overnight with the primary antibodies including RhoA, p-MLC, MLC (Abcam, USA), p-MYPT1, and MYPT1 (Thermo Fisher Scientific, USA) at 4°C. Then, the membranes were washed three times with Tris Buffered Saline with Tween (TBST) and incubated with the secondary antibody for 1 hour. Last, the protein expression was measured using enhanced chemiluminescence reagents. GAPDH protein was used as reference. The bands were imaged, and the optical density of band was quantified using ImageJ software (National Institutes of Health, USA).

Transcriptome sequencing and data analysis

Two milliliters of macrophage cell suspension (1×10^4 cells/ml) was cultured with different samples in a six-well plate for 48 hours. Then, the macrophages were lysed by trizol reagent (Beyotime Biotechnology), and cell lysates were stored at −80°C before sequencing. RNA sequencing was performed using an Illumina HiSeq X10 (Illumina, USA). The value of gene expression was transformed as $\log_{10}$[TPM (Transcripts Per Million reads) + 1]. The GO and KEGG pathway enrichment analyses were performed using the free online platform of Majorbio Cloud Platform (www.majorbio.com).

In vivo evaluation

A rat tibia implantation model was used to evaluate the immune response and osteointegration around the 90-nm and 5-μm samples with unpatterned Ti as the control group ($n = 3$). Male Sprague-Dawley rats weighing 350 to 400 g were obtained from Hubei Province Centers

for Disease Prevention and Control. The animal experiment protocols were approved by the animal research committee of Tongji Medical College, Huazhong University of Science and Technology, Wuhan, China. The rods of unpatterned Ti, 90 nm and 5 μm, were sterilized before implantation. Rats were randomly divided into three groups for implantation with the three different rods mentioned above ($n = 3$). Before surgery, the rats were anesthetized with pentobarbital [30 mg/kg, 1% (w/w)]. For each group, rod samples were then implanted into the tibial plateaus of both legs. To evaluate the initial plasma protein absorption, the animals were euthanized after 8 hours of surgery by using an anesthetic overdose. The implanted samples were harvested from the tibia and rinsed by PBS for three times to remove unattached proteins. The concentration of absorbed protein was then measured by commercial ELISA kits (Wuhan Baiqiandu Technology Co. Ltd. Wuhan, China) under the manufacturer's guidance. To evaluate bone-to-implant osteointegration, the animals were euthanized 4 weeks after implantation by using an anesthetic overdose, and the tibias with implants were harvested for further analysis.

Micro-CT analysis

Tibias with implants were first scanned using a micro-CT system (SKYSCAN, 1076, SkyScan, Belgium). The obtained scanning images were 3D reconstructed using CTVol software (SkyScan). The percentages of new bone volume (BV/TV) were characterized by using CTAn software (SkyScan).

Histological characteristics

After micro-CT scanning, the harvested tibias with implants were processed for immunohistochemistry staining and Van Gieson's picrofuchsin staining. Tissue morphologies were imaged by a Pannoramic Digital Slide Scanner (3DHISTECH, Hungary) and analyzed using Pannoramic Viewer software (3DHISTECH, Hungary).

Statistical analysis

Each experiment was evaluated as mean values ± SD of at least three tests. A one-way analysis of variance (ANOVA) program combined with a Student t test was used to evaluate the statistical significance of the variance. Values of $^{*}P < 0.05$ and $^{**}P < 0.01$ were considered statistically significant.

SUPPLEMENTARY MATERIALS

Supplementary material for this article is available at http://advances.sciencemag.org/cgi/content/full/7/14/eabf6654/DC1

View/request a protocol for this paper from *Bio-protocol*.

REFERENCES AND NOTES

1. R. Londono, S. F. Badylak, Biologic scaffolds for regenerative medicine: Mechanisms of *in vivo* remodeling. *Ann. Biomed. Eng.* **43**, 577–592 (2015).
2. J. M. Anderson, A. Rodriguez, D. T. Chang, Foreign body reaction to biomaterials. *Semin. Immunol.* **20**, 86–100 (2008).
3. S. A. Eming, T. Krieg, J. M. Davidson, Inflammation in wound repair: Molecular and cellular mechanisms. *J. Invest. Dermatol.* **127**, 514–525 (2007).
4. F. Y. McWhorter, C. T. Davis, W. F. Liu, Physical and mechanical regulation of macrophage phenotype and function. *Cell. Mol. Life Sci.* **72**, 1303–1316 (2015).
5. P. Guihard, Y. Danger, B. Brounais, E. David, R. Brion, J. Delecrin, C. D. Richards, S. Chevalier, F. Rédini, D. Heymann, H. Gascan, F. Blanchard, Induction of osteogenesis in mesenchymal stem cells by activated monocytes/macrophages depends on oncostatin M signaling. *Stem Cells* **30**, 762–772 (2012).
6. Q.-l. Ma, L. Fang, N. Jiang, L. Zhang, Y. Wang, Y.-m. Zhang, L.-h. Chen, Bone mesenchymal stem cell secretion of sRANKL/OPG/M-CSF in response to macrophage-mediated inflammatory response influences osteogenesis on nanostructured Ti surfaces. *Biomaterials* **154**, 234–247 (2018).
7. J.-l. Sun, K. Jiao, L. N. Niu, Y. Jiao, Q. Song, L.-j. Shen, F. R. Tay, J.-h. Chen, Intrafibrillar silicified collagen scaffold modulates monocyte to promote cell homing, angiogenesis and bone regeneration. *Biomaterials* **113**, 203–216 (2017).
8. C. Shi, E. G. Pamer, Monocyte recruitment during infection and inflammation. *Nat. Rev. Immunol.* **11**, 762–774 (2011).
9. S. Chen, J. A. Jones, Y. Xu, H.-Y. Low, J. M. Anderson, K. W. Leong, Characterization of topographical effects on macrophage behavior in a foreign body response model. *Biomaterials* **31**, 3479–3491 (2010).
10. K. Garg, N. A. Pullen, C. A. Oskeritzian, J. J. Ryan, G. L. Bowlin, Macrophage functional polarization (M1/M2) in response to varying fiber and pore dimensions of electrospun scaffolds. *Biomaterials* **34**, 4439–4451 (2013).
11. S.-S. Jin, D.-Q. He, D. Luo, Y. Wang, M. Yu, B. Guan, Y. Fu, Z.-X. Li, T. Zhang, Y.-H. Zhou, C.-Y. Wang, Y. Liu, A biomimetic hierarchical nanointerface orchestrates macrophage polarization and mesenchymal stem cell recruitment to promote endogenous bone regeneration. *ACS Nano* **13**, 6581–6595 (2019).
12. O. R. Mahon, D. C. Browe, T. Gonzalez-Fernandez, P. Pitacco, I. T. Whelan, S. V. Euw, C. Hobbs, V. Nicolosi, K. T. Cunningham, K. H. G. Mills, D. J. Kelly, A. Dunne, Nano-particle mediated M2 macrophage polarization enhances bone formation and MSC osteogenesis in an IL-10 dependent manner. *Biomaterials* **239**, 119833 (2020).
13. B. N. Brown, J. E. Valentin, A. M. Stewart-Akers, G. P. McCabe, S. F. Badylak, Macrophage phenotype and remodeling outcomes in response to biologic scaffolds with and without a cellular component. *Biomaterials* **30**, 1482–1491 (2009).
14. B. N. Brown, R. Londono, S. Tottey, L. Zhang, K. A. Kukla, M. T. Wolf, K. A. Daly, J. E. Reing, S. F. Badylak, Macrophage phenotype as a predictor of constructive remodeling following the implantation of biologically derived surgical mesh materials. *Acta Biomater.* **8**, 978–987 (2012).
15. C. Schlundt, T. E. Khassawna, A. Serra, A. Dienelt, S. Wendler, H. Schell, N. van Rooijen, A. Radbruch, R. Lucius, S. Hartmann, G. N. Duda, K. Schmidt-Bleek, Macrophages in bone fracture healing: Their essential role in endochondral ossification. *Bone* **106**, 78–89 (2018).
16. J. Li, J. Wen, B. Li, W. Li, W. Qiao, J. Shen, W. Jin, X. Jiang, K. W. K. Yeung, P. K. Chu, Valence state manipulation of cerium oxide nanoparticles on a titanium surface for modulating cell fate and bone formation. *Adv. Sci.* **5**, 1700678 (2018).
17. Z. Chen, A. Bachhuka, S. Han, F. Wei, S. Lu, R. M. Visalakshan, K. Vasilev, Y. Xiao, Tuning chemistry and topography of nanoengineered surfaces to manipulate immune response for bone regeneration applications. *ACS Nano* **11**, 4494–4506 (2017).
18. B. N. Brown, B. D. Ratner, S. B. Goodman, S. Amar, S. F. Badylak, Macrophage polarization: An opportunity for improved outcomes in biomaterials and regenerative medicine. *Biomaterials* **33**, 3792–3802 (2012).
19. I. Cockerill, Y. Su, J. H. Lee, D. Berman, M. L. Young, Y. Zheng, D. Zhu, Micro–/nanotopography on bioresorbable zinc dictates cytocompatibility, bone cell differentiation, and macrophage polarization. *Nano Lett.* **20**, 4594–4602 (2020).
20. J. Wang, F. Meng, W. Song, J. Jin, Q. Ma, D. Fei, L. Fang, L. Chen, Q. Wang, Y. Zhang, Nanostructured titanium regulates osseointegration via influencing macrophage polarization in the osteogenic environment. *Int. J. Nanomedicine* **13**, 4029–4043 (2018).
21. Z. Zhang, Y. Xie, H. Pan, L. Huang, X. Zheng, Influence of patterned titanium coatings on polarization of macrophage and osteogenic differentiation of bone marrow stem cells. *J. Biomater. Appl.* **32**, 977–986 (2018).
22. D. Karazisis, S. Petronis, H. Agheli, L. Emanuelsson, B. Norlindh, A. Johansson, L. Rasmusson, P. Thomsen, O. Omar, The influence of controlled surface nanotopography on the early biological events of osseointegration. *Acta Biomater.* **53**, 559–571 (2017).
23. Z. Chen, S. Ni, S. Han, R. Crawford, S. Lu, F. Wei, J. Chang, C. Wu, Y. Xiao, Nanoporous microstructures mediate osteogenesis by modulating the osteo-immune response of macrophages. *Nanoscale* **9**, 706–718 (2017).
24. F. Y. McWhorter, T. Wang, P. Nguyen, T. Chung, W. F. Liu, Modulation of macrophage phenotype by cell shape. *Proc. Natl. Acad. Sci. U.S.A.* **110**, 17253–17258 (2013).
25. J. Wang, S. Qian, X. Liu, L. Xu, X. Miao, Z. Xu, L. Cao, H. Wang, X. Jiang, M2 macrophages contribute to osteogenesis and angiogenesis on nanotubular TiO_2 surfaces. *J. Mater. Chem. B* **5**, 3364–3376 (2017).
26. T. U. Luu, S. C. Gott, B. W. Woo, M. P. Rao, W. F. Liu, Micro- and nanopatterned topographical cues for regulating macrophage cell shape and phenotype. *ACS Appl. Mater. Interfaces* **7**, 28665–28672 (2015).
27. T. Tylek, C. Blum, A. Hrynevich, K. Schlegelmilch, T. Schilling, P. D. Dalton, J. Groll, Precisely defined fiber scaffolds with 40μm porosity induce elongation driven M2-like polarization of human macrophages. *Biofabrication* **12**, 025007 (2020).
28. Q. L. Ma, L. Z. Zhao, R. R. Liu, B. Q. Jin, W. Song, Y. Wang, Y. S. Zhang, L. H. Chen, Y. M. Zhang, Improved implant osseointegration of a nanostructured titanium surface via mediation of macrophage polarization. *Biomaterials* **35**, 9853–9867 (2014).
29. P. Kanchanawong, G. Shtengel, A. Pasapera, E. Ramko, M. Davidson, H. Hess, C. Waterman, Nanoscale architecture of integrin-based cell adhesions. *Nature* **468**, 580–584 (2010).

30. M. J. Dalby, N. Gadegaard, R. O. Oreffo, Harnessing nanotopography and integrin-matrix interactions to influence stem cell fate. *Nat. Mater.* **13**, 558–569 (2014).
31. N. Jain, V. Vogel, Spatial confinement downsizes the inflammatory response of macrophages. *Nat. Mater.* **17**, 1134–1144 (2018).
32. A. K. Azad, M. V. Rajaram, L. S. Schlesinger, Exploitation of the macrophage mannose receptor (CD206) in infectious disease diagnostics and therapeutics. *J Cytol Mol Biol* **1**, 1000003 (2014).
33. Z. J. Xu, Y. Gu, C. Z. Wang, Y. Jin, X. M. Wen, J. C. Ma, L. J. Tang, Z. W. Mao, J. Qian, J. Lin, The M2 macrophage marker CD206: a novel prognostic indicator for acute myeloid leukemia. *Onco. Targets. Ther.* **9**, 1683347 (2020).
34. F. Wei, Y. Zhou, J. Wang, C. Liu, Y. Xiao, The immunomodulatory role of BMP-2 on macrophages to accelerate osteogenesis. *Tissue Eng. Part A* **24**, 584–594 (2018).
35. P. Guihard, M. A. Boutet, B. Brounais-Le Royer, A. L. Gamblin, J. Amiaud, A. Renaud, M. Berreur, F. Redini, D. Heymann, P. Layrolle, F. Blanchard, Oncostatin M, an inflammatory cytokine produced by macrophages, supports intramembranous bone healing in a mouse model of tibia injury. *Am. J. Pathol.* **185**, 765–775 (2015).
36. Y. Zhang, T. Bose, R. E. Unger, J. A. Jansen, C. J. Kirkpatrick, J. J. J. P. van den Beucken, Macrophage type modulates osteogenic differentiation of adipose tissue MSCs. *Cell Tissue Res.* **369**, 273–286 (2017).
37. S. S. Singh, A. Roy, B. E. Lee, I. Banerjee, P. N. Kumta, MC3T3-E1 proliferation and differentiation on biphasic mixtures of Mg substituted β-tricalcium phosphate and amorphous calcium phosphate. *Mater. Sci. Eng. C* **45**, 589–598 (2014).
38. Z. Chen, T. Klein, R. Z. Murray, R. Crawford, J. Chang, C. Wu, Y. Xiao, Osteoimmunomodulation for the development of advanced bone biomaterials. *Mater. Today* **19**, 304–321 (2016).
39. P. Qiu, M. Li, K. Chen, B. Fang, P. Chen, Z. Tang, X. Lin, S. Fan, Periosteal matrix-derived hydrogel promotes bone repair through an early immune regulation coupled with enhanced angio- and osteogenesis. *Biomaterials* **227**, 119552 (2020).
40. F. M. Szaba, S. T. Smiley, Roles for thrombin and fibrin(ogen) in cytokine/chemokine production and macrophage adhesion in vivo. *Blood* **99**, 1053–1059 (2002).
41. W. J. Hu, J. W. Eaton, T. P. Ugarova, L. Tang, Molecular basis of biomaterial-mediated foreign body reactions. *Blood* **98**, 1231–1238 (2001).
42. J. Maciel, M. I. Oliveira, E. Colton, A. K. McNally, C. Oliveira, J. M. Anderson, M. A. Barbosa, Adsorbed fibrinogen enhances production of bone- and angiogenic-related factors by monocytes/macrophages. *Tissue Eng. Part A* **20**, 250–263 (2014).
43. K. L. Kilpadi, P. L. Chang, S. L. Bellis, Hydroxylapatite binds more serum proteins, purified integrins, and osteoblast precursor cells than titanium or steel. *J. Biomed. Mater. Res.* **57**, 258–267 (2001).
44. G. A. Pilz, C. Ulrich, M. Ruh, H. Abele, R. Schäfer, T. Kluba, H. J. Bühring, B. Rolauffs, W. K. Aicher, Human term placenta-derived mesenchymal stromal cells are less prone to osteogenic differentiation than bone marrow-derived mesenchymal stromal cells. *Stem Cells Dev.* **20**, 635–646 (2011).
45. J. Loeffler, G. N. Duda, F. A. Sass, A. Dienelt, The metabolic microenvironment steers bone tissue regeneration. *Trends Endocrinol. Metab.* **29**, 99–110 (2018).
46. Q. Yao, J. Liu, Z. Zhang, F. Li, C. Zhang, B. Lai, L. Xiao, N. Wang, Peroxisome proliferator-activated receptor γ (PPARγ) induces the gene expression of integrin αVβ5 to promote macrophage M2 polarization. *J. Biol. Chem.* **293**, 16572–16582 (2018).
47. R. H. Deng, M. Z. Zou, D. Zheng, S. Y. Peng, W. Liu, X. F. Bai, H. S. Chen, Y. Sun, P. H. Zhou, X. Z. Zhang, Nanoparticles from cuttlefish ink inhibit tumor growth by synergizing immunotherapy and photothermal therapy. *ACS Nano* **13**, 8618–8629 (2019).
48. H. Zhou, A. P. Coveney, M. Wu, J. Huang, S. Blankson, H. Zhao, D. P. O'Leary, Z. Bai, Y. Li, H. P. Redmond, J. H. Wang, J. Wang, Activation of both TLR and NOD Signaling confers host innate immunity-mediated protection against microbial infection. *Front. Immunol.* **9**, 3082 (2018).
49. T.-M. Wu, F.-H. Nan, K.-C. Chen, Y.-S. Wu, Sarcodia suieae acetyl-xylogalactan regulate RAW 264.7 macrophage NF-kappa B activation and IL-1 beta cytokine production in macrophage polarization. *Sci. Rep.* **9**, 19627 (2019).
50. D. Chen, J. Xie, R. Fiskesund, W. Dong, X. Liang, J. Lv, X. Jin, J. Liu, S. Mo, T. Zhang, F. Cheng, Y. Zhou, H. Zhang, K. Tang, J. Ma, Y. Liu, B. Huang, Chloroquine modulates antitumor immune response by resetting tumor-associated macrophages toward M1 phenotype. *Nat. Commun.* **9**, 873 (2018).
51. A. D. Luster, R. Alon, U. H. von Andrian, Immune cell migration in inflammation: present and future therapeutic targets. *Nat. Immunol.* **6**, 1182–1190 (2005).
52. G. Berton, C. A. Lowell, Integrin signaling in neutrophils and macrophages. *Cell. Signal.* **11**, 621–635 (1999).
53. P. Friedl, B. Weigelin, Interstitial leukocyte migration and immune function. *Nat. Immunol.* **9**, 960–969 (2008).
54. L. T. Duong, G. A. Rodan, PYK2 is an adhesion kinase in macrophages, localized in podosomes and activated by beta(2)-integrin ligation. *Cell Motil. Cytoskeleton* **47**, 174–188 (2000).
55. L. Lv, Y. Xie, K. Li, T. Hu, X. Lu, Y. Cao, X. Zheng, Zheng, Unveiling the mechanism of surface hydrophilicity-modulated macrophage polarization. *Adv. Healthc. Mater.* **7**, e1800675 (2018).
56. B. H. Cha, S. R. Shin, J. Leijten, Y. C. Li, S. Singh, J. C. Liu, N. Annabi, R. Abdi, M. R. Dokmeci, N. E. Vrana, A. M. Ghaemmaghami, A. Khademhosseini, Integrin-mediated interactions control macrophage polarization in 3D hydrogels. *Adv. Healthc. Mater.* **6**, 1700289 (2017).
57. D. A. Murphy, S. A. Courtneidge, The 'ins' and 'outs' of podosomes and invadopodia: characteristics, formation and function. *Nat. Rev. Mol. Cell Biol.* **12**, 413–426 (2011).
58. R. Zaidel-Bar, M. Cohen, L. Addadi, B. Geiger, Hierarchical assembly of cell–matrix adhesion complexes. *Biochem. Soc. Trans.* **32**, 416–420 (2004).
59. A. Hall, Rho GTPases and the actin cytoskeleton. *Science* **279**, 509–514 (1998).
60. Y. Xu, K. Cui, J. Li, X. Tang, J. Lin, X. Lu, R. Huang, B. Yang, Y. Shi, D. Ye, J. Huang, S. Yu, X. Liang, Melatonin attenuates choroidal neovascularization by regulating macrophage/microglia polarization via inhibition of RhoA/ROCK signaling pathway. *J. Pineal Res.* **69**, e12660 (2020).

Acknowledgments

Funding: This work is jointly supported by National Key R&D Program of China (2018YFA0703100), General Research Fund of Hong Kong Research Grant Council (nos. 17207719 and 17214516), Hong Kong Health and Medical Research Fund (no.19180712), the National Science Fund for Distinguished Youth Scholar (no. 51925104), Shenzhen Science and Technology Funding (JSGG20180507183242702), HKU-SZH Fund for Shenzhen Key Medical Discipline (SZXK2020084), and Sanming Project of Medicine in Shenzhen "Team of Excellence in Spinal Deformities and Spinal Degeneration" (SZSM201612055). We thank Wuhan Union Hospital also for their collaboration and assistance with this animal experiments research.

Author contributions: Y.Z., X.L., S.W., and K.W.K.Y. conceived and designed the concept of the experiments. Y.Z. and H.L. synthesized the materials and conducted the material characterizations. Y.Z., H.L., X.L., S.W., C.Y., and K.W.K.Y. analyzed the experimental data and cowrote the manuscript. X.L., J.W., C.Y., T.M.W., K.Y.H.K., K.M.C.C., S.W., and K.W.K.Y. provided important experimental insights. All the authors discussed, commented, and agreed on the manuscript. **Competing interests:** The authors declare that they have no competing interests. **Data and materials availability:** All data needed to evaluate the conclusions in the paper are present in the paper and/or the Supplementary Materials. Additional data related to this paper may be requested from the authors.

Submitted 11 November 2020
Accepted 17 February 2021
Published 2 April 2021
10.1126/sciadv.abf6654

Citation: Y. Zhu, H. Liang, X. Liu, J. Wu, C. Yang, T. M. Wong, K. Y. H. Kwan, K. M. C. Cheung, S. Wu, K. W. K. Yeung, Regulation of macrophage polarization through surface topography design to facilitate implant-to-bone osteointegration. *Sci. Adv.* **7**, eabf6654 (2021).